AlN-AlN Layer Bonding and Its Thermal Characteristics

S. Bao,[a,b,*] K. H. Lee,[a] G. Y. Chong,[b] E. A. Fitzgerald,[a,c] and C. S. Tan[a,b,z]

[a]*Singapore-MIT Alliance for Research and Technology (SMART), Singapore 138602*
[b]*School of Electrical and Electronic Engineering, Nanyang Technological University, Singapore 639798*
[c]*Department of Materials Science and Engineering, Massachusetts Institute of Technology, Cambridge, Massachusetts 02139, USA*

Homogeneous bonding was successfully demonstrated on 150 mm Si wafers by face-to-face direct dielectric bonding of clean and smooth aluminum nitride (AlN) layers. Characterization result from XPS confirms the layer composition and reveals that approximately 5 nm of the layer surface was partially oxidized during processing. After activation, substoichiometric nitrogen bound to aluminum, Al-O and Al-OH bonds were found at the thin film surface. The as-bonded wafer pairs are nearly void and particle free with a high bonding strength of 1527.8 ± 272.2 mJ/m^2, enabling them to withstand the subsequent process steps. In addition, experimental results have indicated that the AlN-AlN bonded wafers can achieve a 23 and 16% improvement respectively in terms of heat dissipation compared with those using SiO_2 and Al_2O_3 as the bonding layer. It is concluded that this AlN-AlN bonded wafer pairs can exhibit a better heat dissipation capability than other bonded counterparts.
© The Author(s) 2015. Published by ECS. This is an open access article distributed under the terms of the Creative Commons Attribution 4.0 License (CC BY, http://creativecommons.org/licenses/by/4.0/), which permits unrestricted reuse of the work in any medium, provided the original work is properly cited. [DOI: 10.1149/2.0121507jss] All rights reserved.

Manuscript submitted January 16, 2015; revised manuscript received April 15, 2015. Published April 24, 2015. This was Paper 1730 presented at the Cancun, Mexico, Meeting of the Society, October 5–9, 2014.

Wafer bonding allows heterogeneous integration of two materials that have similar or very different lattice parameters and thermal properties, via an intermediate bonding layer or direct bonding. One of the most prominent applications of wafer bonding is silicon-on-insulator (SOI),[1–5] and it can also be extended to germanium-on-insulator (GOI)[6,7] or other III-V groups integration.[8,9] First direct bonded SOI was reported by Lasky et al. in 1986. Since then, SOI fabricated from wafer bonding has been gaining ground from the conventional Si substrate in ultra-large scale integrations (ULSI) and micro-electro-mechanical systems (MEMS)[10] as the starting substrate, which benefits from its on-insulator structure. The "on-insulator" advantages make it possible to attain mechanical stability close to Si substrate and excellent electrostatic control, such as attenuated short-channel effects,[11] reduced parasitic capacitance and absence of latch-up.[12] As the most common buried insulator material, SiO_2 has already shown extensive popularity in a couple of optical devices.[13–15] However, the low thermal conductivity of SiO_2 (1.46 Wm^{-1} K^{-1}) limits the heat dissipation efficiency and degrades the advantages of SOI. Also, the degraded heat dissipation path deteriorates its heat transfer efficiency to the underlying bulk Si layer, leading to severe self-heating effect. This effect is further magnified by device scaling for performance improvement, which constrains the applicability of SOI in electronics, especially in the cases where high temperature and power dissipation are expected. In order to address this problem, numerous efforts have been dedicated to exploring for novel buried insulator materials with high thermal conductivity such as diamond and silicon carbide.[16] Liang et al. had demonstrated the outstanding heat dissipation advantage of silicon-on-diamond (SOD) comparing to the conventional SOI substrate.[17] Furthermore, high-k dielectric materials with high thermal conductivity have drawn great attention in SOI fabrication. For example, Puurunen et al. had confirmed the possibility to utilize TiO_2 as the buried insulator in the formation of SOI by wafer bonding, whereas an Al_2O_3 under-layer was required.[18] Additionally, SOI formed through Al_2O_3-Al_2O_3 bonding was successfully demonstrated.[4] This was accomplished with the assistance of surface activation carried out at room temperature. Besides TiO_2 and Al_2O_3, another promising candidate is AlN, which has excellent properties including high thermal stability, good dielectric properties and excellent heat dissipation capability with a thermal conductivity of 134 Wm^{-1} K^{-1}.[19] Moreover, its thermal expansion coefficient is close to that of silicon,[20] thus the thermally induced stress can be potentially relieved. Furthermore, its feasibility as a buried insulator layer for SOI had been proven from bondability and heat transfer efficiency aspects via AlN/Si bonding.[21,22]

In this paper, the AlN-AlN direct bonding is investigated to determine its elemental composition and bonding quality as well as to verify its superiority as the buried insulator in terms of heat dissipation capability. Seamless wafer bonding has been successfully demonstrated on 150 mm Si wafer. It provides a possibility to fabricate bonded wafers with enhanced thermal conductivity through room temperature AlN-AlN direct bonding. Its promising heat dissipation capability is verified by COMSOL multi-physic simulation and experimental results obtained from resistance thermal detector (RTD).

Experimental

AlN-AlN layer bonding.— All Si wafers used for bonding were p-type, 150 mm Si (100) test grade wafers, thickness of 625 ± 25 μm, total thickness variation (TTV) < 10 μm and with the resistivity in the range of 10–20 Ω · cm. Firstly, the wafers were pre-cleaned by the standard RCA cleaning method for the purpose of organic and metallic contaminants removal. Then, a 20 nm AlN thin film was deposited onto the pre-cleaned Si surface by sputtering aluminum in N_2 atmosphere at 75°C. While for comparative study, a 20 nm of SiO_2 and Al_2O_3 were deposited via PECVD and ALD system, respectively. After deposition, a pre-annealing step was provided to densify the AlN thin film, allowing outgassing of the incorporated gases. This process helps to eliminate voids formation at the bonding interface in the subsequent processes and is significantly important to improve the bonding quality. The pre-annealing was carried out at 450°C for 1 hr. During pre-annealing, the furnace was purged with N_2 gas to minimize the contact with air or moisture. Next, the pre-annealed wafers underwent 15 s Ar plasma activation for surface hydrophilicity enhancement. They were subsequently cleaned by de-ionized (DI) water rinse and dried with spin dryer. Prior to the bonding, the properties of AlN thin film, such as film composition and roughness, were measured by X-ray photoelectron spectroscopy (XPS) and atomic force microscope (AFM). AlN-AlN layer bonding was initiated at room temperature and atmospheric pressure. Then, the bond was strengthened by annealing at 300°C in N_2 ambient for a duration of 3 hr. The formation process of AlN-AlN layer bonding is illustrated in Figure 1. The bonding quality was verified by both infrared (IR) imaging and cross-sectional transmission electron microscope (X-TEM), while the post-annealing bonding strength was calculated based on Maszara's crack opening method.[23]

Thermal characteristics measurement.— After the bond strengthening annealing, Si on one side of the bonded structure was removed

*Electrochemical Society Student Member.
zE-mail: tancs@ntu.edu.sg

Downloaded on 2015-06-08 to IP 155.69.250.85 address. Redistribution subject to ECS terms of use (see ecsdl.org/site/terms_use) unless CC License in place (see abstract).

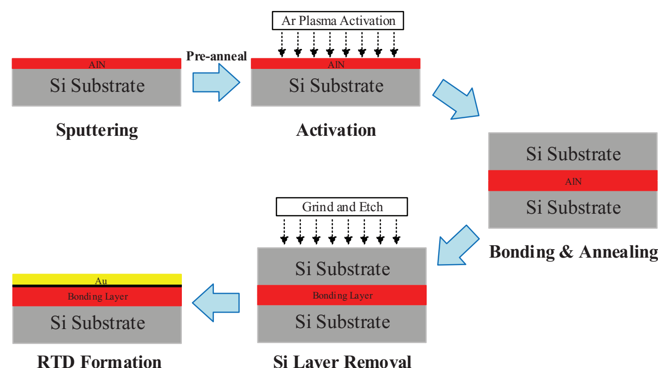

Figure 1. Formation process for AlN-AlN layer bonding and RTD on the bonded wafers.

by grinding and wet etching. Next, RTD patterns using gold (Au) lines, in the form of Kelvin structures, were formed through lithography, metal deposition, and lift-off processes. Figure 2 depicts the top-view of this RTD pattern and the dimension of zig-zag line in the pattern was 1445 μm in length, 15 μm in width, and the thickness of Au line was 150 nm. Here, a 30 nm thick chrome layer was used to promote the adhesion. Then, *I-V* measurement was carried out on these RTDs to verify the thermal characteristics of the bonding layers.

It is well-known that Au resistivity increases with temperature in a linear fashion.[24] Hence, by measuring the resistance of RTD pattern formed from Au line Kelvin structures, the temperature variation can be easily estimated. In the *I-V* measurement, a small current I was applied across the RTD, and voltages at two terminals of the pattern was denoted as V_1 and V_2. Thus, the RTD's resistance can be calculated from the following equation:

$$R = \frac{V_1 - V_2}{I}. \quad [1]$$

Then, the resistance dependency on temperature was measured between 25 to 150°C with a temperature increment of 25°C/step. The injected stressing current was 5 mA to minimize the self-heating effect. After that, a linear approximation between the resistance of RTD and temperature was done by fitting into the equation, expressed as:

$$R_{(T)} = R_{(T_0)} + a(T - T_0) \quad [2]$$

where $R_{(T)}$ and $R_{(T_0)}$ are the resistances measured at temperature T and T_0, respectively; and a is the slope of this linear approximation. Here, T_0 was set at the room temperature (25°C). Later, RTD was subjected to a stressing current in the range of 5–100 mA at room temperature with a 5 mA incremental interval. Its resistance at various stressing current was calculated and calibrated into the linear fitted equation. As a result, the calibrated temperature of RTD as a function of applied power induced by self-heating of the zig-zag Au line was obtained. The resultant temperature deviation in RTD can be utilized as the gauge of heat dissipation capability, where a small deviation stands for an excellent heat dissipation capability.

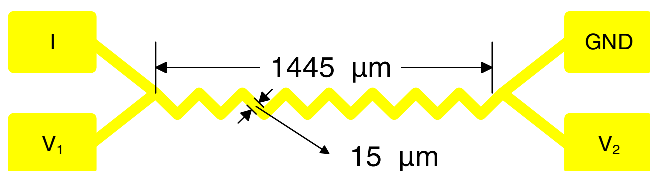

Figure 2. Top-view of the RTD pattern for thermal characteristics measurement.

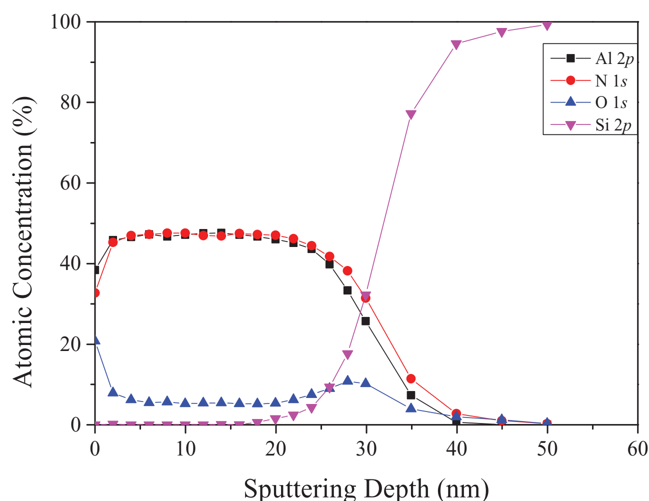

Figure 3. Atomic concentration profiles of pre-annealed AlN sample by XPS.

Results and Discussion

AlN film composition.— XPS measurement was performed to verify the composition of AlN thin film. Owing to the sputter deposition method, a large amount of gases was incorporated in the thin film. These gases would out-diffuse and cause the formation of voids when the annealing temperature is above 100°C. With the increasing annealing time and temperature, the voids are enlarged and finally lead to large debonded areas around the wafer center region. In order to eliminate voids formation, a pre-annealing process was provided at 450°C. However, it is reported that the AlN thin film is prone to oxidation when exposed to air.[25] Moreover, annealing at a high temperature accelerates the oxidation. With these concerns, XPS was carried out on a 30 nm-thick pre-annealed AlN thin film sample using monochromatic Al K-α source for composition examination. From the obtained atomic concentration diagram shown in Figure 3, the atomic ratio between Al and N within the film is nearly 1:1, which confirms that the sputtered film is stoichiometrically matched to that of AlN. However, there is a slight mismatch in the stoichiometry at the surface region, where the oxygen concentration is 20.8 at%. This indicates that the AlN thin film was partially oxidized by H_2O or O_2 in the air and/or air leakage into the N_2 furnace. When the film is sputter-etched, the atomic concentration of oxygen drops to 5.2-5.7 at%. The possible sources introducing oxygen into the thin film are the impurities from source materials and gas incorporation during sputtering caused by the relatively high chamber pressure.

Figure 4 and 5 show the XPS spectra of Al 2*p* and N 1*s* measured at the film surface and within the film of pre-annealed and activated samples. All the results were calibrated against C 1*s* peak at 284.6 eV. Each plot of Al 2*p* peak is deconvoluted into two distinct sub-peaks, noted as sub-peak #1 at 73.6 ± 0.1 eV and sub-peak #2 at 74.6 ± 0.6 eV. Since it is anticipated that the sputtered film is AlN, the dominant sub-peak #1 is thus assigned to aluminum bound to nitrogen, coinciding with previously reported values.[22,26] The sub-peak #2 which has a higher binding energy is assigned to Al-O binding because of the strong electron withdrawing capability of oxygen. Moreover, this peak is close to the reported binding energy of Al-O in aluminum oxide and hydroxides,[27] supporting this assignment. The emergence of Al-O bonds can be attributed to two reasons: a) surface exposure to H_2O or O_2 and annealing accelerated oxidation; and b) plasma activation induced bond defects which facilitate oxygen incorporation to aluminum. Owing to the conjunction effect of surface oxidation and plasma activation, Al 2*p* sub-peak #2 is observed to have the highest intensity at the activated sample surface (shown in Figure 4c) and the lowest intensity within the pre-annealed film (shown in Figure 4b).

Downloaded on 2015-06-08 to IP 155.69.250.85 address. Redistribution subject to ECS terms of use (see ecsdl.org/site/terms_use) unless CC License in place (see abstract).

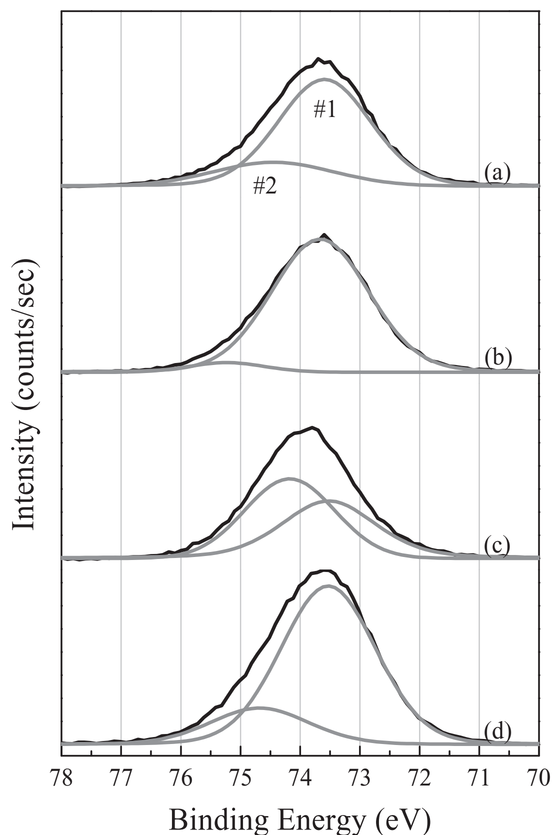

Figure 4. XPS spectra of Al 2*p* peak (a) at the pre-annealed sample surface and (b) within the film, (c) at the activated sample surface and (d) within the film.

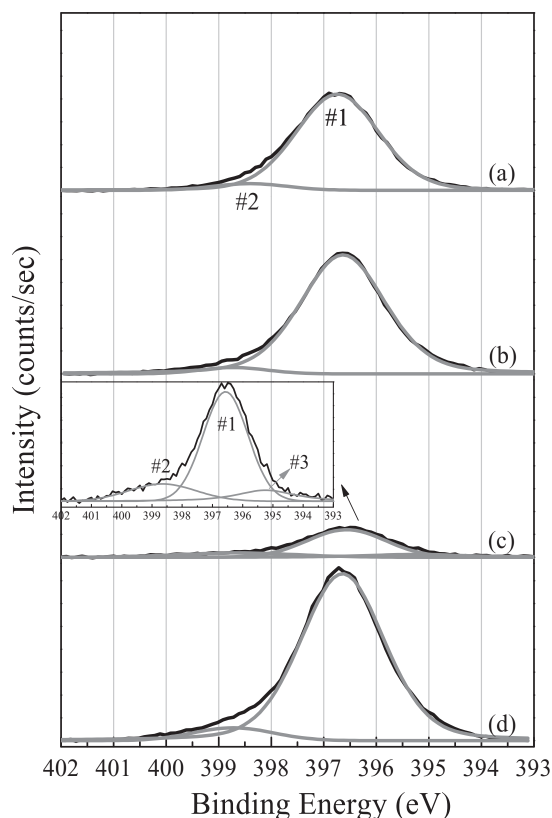

Figure 5. XPS spectra of N 1*s* peak (a) at the pre-annealed sample surface and (b) within the film, (c) at the activated sample surface and (d) within the film.

From Figure 5, two sub-peaks of N 1*s* are at 396.6 ± 0.1 eV and 398.6 ± 0.2 eV. The sub-peak #1 at 396.6 ± 0.1 eV corresponds to nitrogen in AlN.[22,26] The second sub-peak is assigned to nitrogen in the bound state that has a stronger electron withdrawing environment than AlN. It is expected to be in the form of N-Al-O. The FWHM of N 1*s* sub-peak #2 of activated sample surface is found to be broader than the rest. The broadening is due to nitrogen bound to aluminum that has one or more oxygen coordination. Apart from this, another deconvolution of N 1*s* peak at 395.2 eV is observed at the activated film surface. This peak is considered to be substoichiometric nitrogen,[28] which is caused by bond defects induced stoichiometry destruction. However, no N-O bound state is observed, which is reported to be around 403 eV in nitrides and 407 eV in nitrates.[29] Likewise, the absence of N-O bonds in the AlN film has been reported previously.[30]

O 1*s* sub-peak at 531.3 ± 0.3 eV is observed at the surface and within the film, which is assigned to O-Al bond. There is one shoulder with peak centered at 532.4 ± 0.1 eV at the pre-annealed and activated sample surface. It is suspected to be O of OH^- species (in Al-OH bond),[28] which has been reported in boehmite and diaspora.[27,30] Furthermore, the separation between the two O 1*s* spectra here is 1.1 eV, falling in the range of chemical shift between hydroxyl oxygen in hydroxide and O^{2-} oxygen in oxides.[27,31] OH^- species are arisen from the chemisorption of water at the active site of thin film surface.

Therefore, it can be suggested from the XPS results that the surface of AlN thin film consists of substoichiometric nitrogen bound to aluminum, Al-O and Al-OH bonds after plasma activation. In addition, the hydrophilicity is improved, with the contact angle dropping from 36.5° after pre-annealing process to 10.5° after plasma activation. It is because plasma activation can introduce bond defects, resulting in dangling bonds and enhanced chemical reactivity.[32] As a consequence, hydroxyl can easily bond to the active sites of the activated sample surface.[33] This can give rise to a more hydrophilic surface.

Surface roughness.— Direct wafer bonding only occurs between activated wafer pairs when the stringent requirements in surface morphology and roughness are fulfilled. Thus, well control of surface roughness is essential in obtaining successfully bonded wafers, where the root mean square (RMS) roughness needs to be less than 0.5 nm for polar group passivated surface.[34] Smooth and adhesive thin film was sputtered with the RMS of 0.13 nm in a 5 μm × 5 μm AFM scan area as shown in Figure 6a. The roughness value is further reduced to 0.12 nm after the pre-annealing process, which can be seen from Figure 6b. The smoothening in surface roughness is originated from both the surface oxidation process[35] and the removal of incorporated gases. Though Ar plasma activation roughens the surface (shown in Figure 6c), the RMS value of activated surface, which is 0.33 nm, is still within the bonding requirement. Thus, it allows direct wafer bonding when bringing two such wafers into intimate contact.

Bonding quality.— The IR imaging result in Figure 7a shows that AlN thin film exhibits very good bondability when two of them are bonded face-to-face. The good bondability can be attributed to the sufficiently clean and flat surface with low surface roughness. Only very few unbonded areas were observed due to the presence of particles, which were trapped during wafer handling and can be eliminated with careful control of contamination sources. This led to a respectable AlN-AlN bonded interface. After annealing, no obvious void enlargement or new void formation was found, which indicates that out-gassing is not significant. The low out-gassing level is thanks to the pre-annealing process introduced prior to wafer bonding.

As microvoids are not within the detection limit of IR imaging due to its low resolution, X-TEM was employed to detect the voids from microscale. Figure 8 shows the X-TEM image taken from the bonded region center of bond-strengthening annealed wafer pairs. The TEM sample was prepared by focused ion beam (FIB) milling. According to the X-TEM images, it reveals that the bonded layer is uniform

Downloaded on 2015-06-08 to IP 155.69.250.85 address. Redistribution subject to ECS terms of use (see ecsdl.org/site/terms_use) unless CC License in place (see abstract).

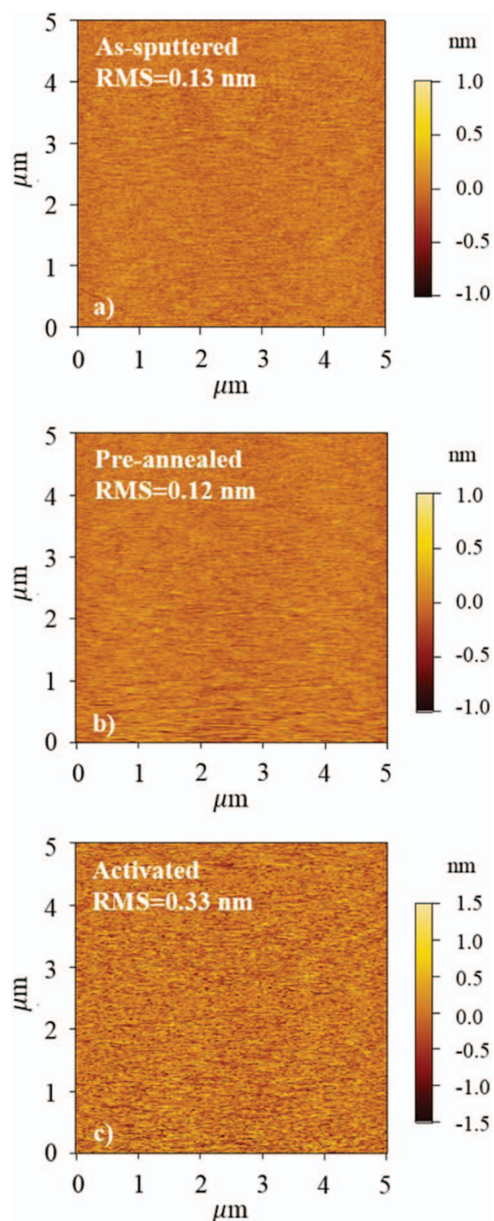

Figure 6. AFM images of (a) as-sputtered, (b) pre-annealed, and (c) activated AlN layer.

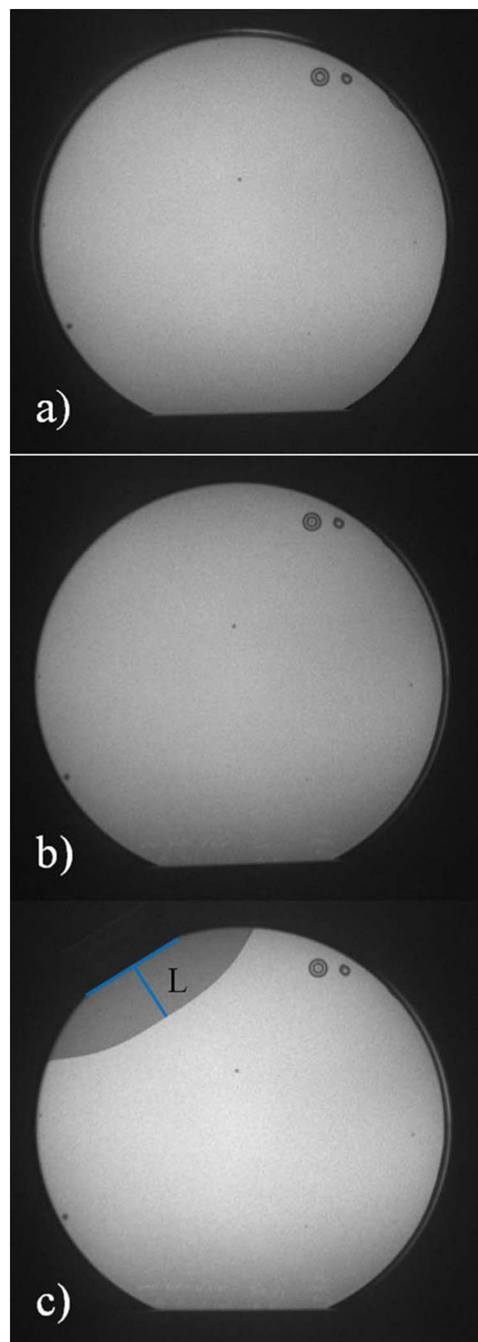

Figure 7. IR images of bonded Si/AlN-AlN/Si wafer (a) before, (b) after bond strengthening annealing in N_2 ambient, and (c) with crack opening.

without defects. This further confirms that a seamless bonding has been successfully achieved. AlN layers were deposited uniformly on each Si wafer with small thickness variation. The total thickness of bonded layer is 23.8 nm. Here, the large difference between measured and target bonded layer thickness was caused by imprecision in sputtering rate. Hence, the calibrated sputtering rate based on the thickness information obtained from TEM was used for AlN thin film deposition in the rest experiments. According to Figure 8, the bonding interface region appears to be brighter (6.1 nm), due to film surface oxidation upon exposing to air and stoichiometry destruction during activation.

Figure 9 plots the EDX line scan result performed across the bonding interface. Based on the result, the bonding interface is AlNO with a high O and low N content. However, the O level is low within the AlN layer. Additionally, slight interdiffusion between AlN and Si is observed. All these results agree with the findings from XPS.

The bonding strength is estimated using the crack opening model. A crack is introduced by inserting a razor blade, thickness of $2y$, into

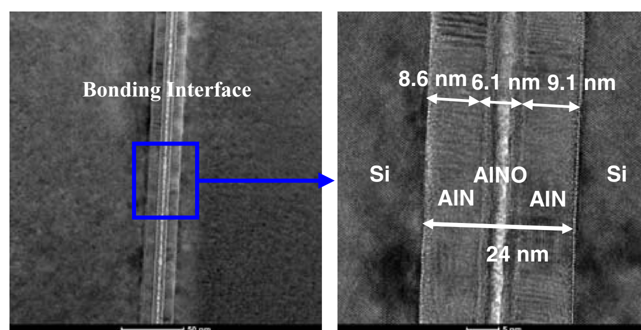

Figure 8. Cross-sectional TEM image of bonded Si/AlN-AlN/Si wafer.

Downloaded on 2015-06-08 to IP 155.69.250.85 address. Redistribution subject to ECS terms of use (see ecsdl.org/site/terms_use) unless CC License in place (see abstract).

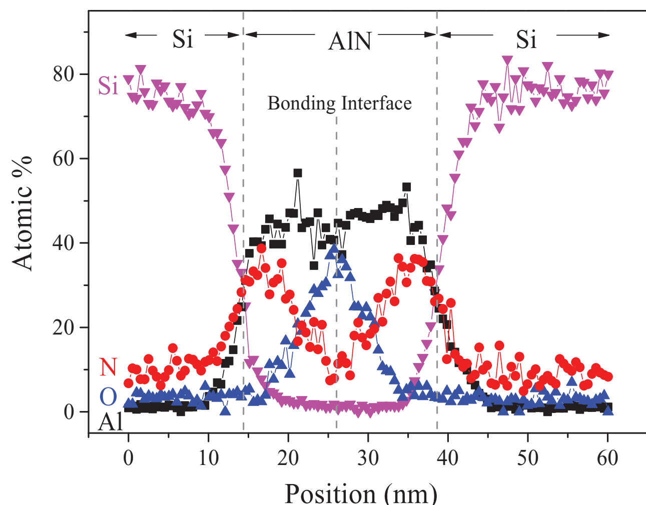

Figure 9. EDX line scan across the bonded Si/AlN-AlN/Si wafer central region.

the edges of the bonded wafer pairs. Then, the crack propagates along the interface, giving rise to a crack length L. The bonding strength γ can be calculated through substituting the value of L into the following equation:[23]

$$\gamma = \frac{3Et^3y^2}{8L^4} \quad [3]$$

where E is the elastic modulus of Si (100), and t is the thickness of a single wafer. Based on this method, the crack length of the bonded sample is 22.6 ± 0.9 mm and the bonding strength is estimated to be 1527.8 ± 272.2 mJ/m^2, which is sufficiently high to withstand the subsequent process steps. It has been proven by the fact that the sample is able to withstand FIB preparation steps without any debonding issue.

Polymerization of M-OHs by hydrogen bonding is one reason for its high bonding strength. Similar to other group III metals, Al behaves less ionic and its hydroxides has strong polarization power.[32] Thus, its hydroxides can polymerize forming strong M-O-M bonding with water molecule as the by-product, which can be expressed as:

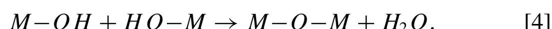

$$M-OH + HO-M \rightarrow M-O-M + H_2O. \quad [4]$$

The resultant water at bonding interface is first absorbed by the amorphous bonding layer, and then diffuses to react with Si under low temperature annealing.[36] Through this bonding interface reaction, H_2O is converted into H_2, which is a small molecule and can diffuse easily along the bonding layer or through Si. However, it is still not clear if there is any reaction between M-NH groups across the bonding interfaces similar to that in Si_3N_4.[32] Since the substoichiometric nitrogen groups formed after activation are non-fully coordinated and chemically reactive, it is anticipated that they are likely to be passivated by H after DI water rinse. Consequently, the surface is covered with M-NH groups. It is possible that they would react and form M-N_x-M bonds with the release of hydrogen.

Thermal characteristics of bonded wafers.— According to the COMSOL multi-physic simulation results, AlN has shown a great advantage as the insulator layer in terms of heat dissipation capability compared with conventional insulator materials SiO_2 and the recently widely studied Al_2O_3. Their heat dissipation capability was investigated and compared by studying the temperature profile across the bonded structure when the material stack was subjected to a heat flux of 1 × 10^8 W/m^2. To reduce the computation load, material stack with 40 nm bonding layer and 10 μm Si substrate was used in this simulation. From Figure 10, the simulated surface temperature of 40 nm SiO_2, Al_2O_3, AlN, Si on Si structures are 35.25, 32.50, 32.42, and 32.42°C, respectively. 40 nm AlN on Si appeared to have the similar temperature profile as direct Si-Si bonded wafers, because they have close thermal conductivity values (AlN: 134 Wm^{-1} K^{-1} and Si: 131 Wm^{-1} K^{-1}). Thus, it can be concluded that the presence of AlN thin film does not degrade the thermal property or hinder heat from spreading to the underlying Si substrate.

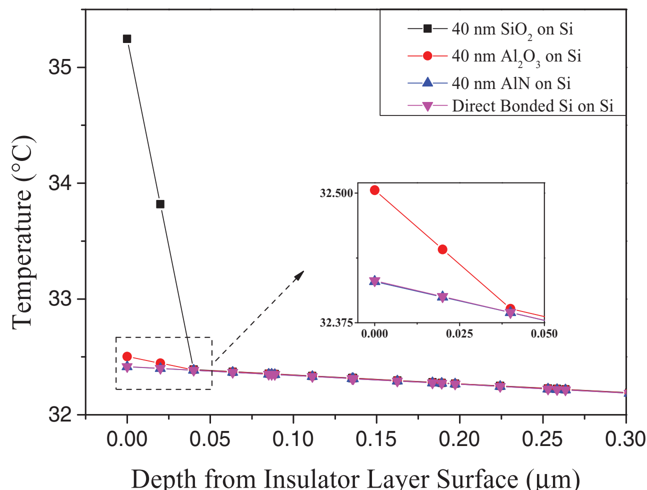

Figure 10. Cross sectional temperature profile of 40 nm SiO_2/Al_2O_3/AlN/Si on Si according to COMSOL multi-physic simulation.

To further confirm the findings from COMSOL multi-physic simulation results, *I-V* measurement was carried out on RTDs that had been formed on the bonded wafers after grinding with three different bonding intermediate layers: SiO_2, Al_2O_3 and AlN. In the *I-V* measurement, each data point took the average from 50 sampling times. Then, the calculated RTD resistance is substituted into the respective linear fitted Eq. 2. Thus, the calibrated temperature increase in RTD under stressing current in the range of 5–100 mA is obtained. Figure 11 shows the measurement results against 5 samples. It can be revealed that the temperature increase in RTD formed on the AlN bonding layer is less obvious than the rest under the same stressing current. When plotting the temperature increase in RTD against supply power density, a linear fitted curve can be obtained (shown in Figure 12). According to the measured data, the samples with RTD on AlN bonding material are estimated to have the smallest temperature increment of 2.98 ± 0.08°C under a supply power density of 1000 W/cm^2, whereas the temperature increase in SiO_2 and Al_2O_3

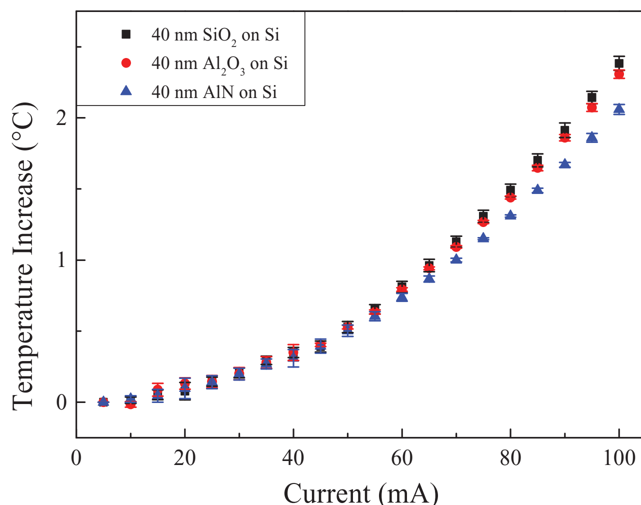

Figure 11. Temperature increase in RTD formed on 40 nm SiO_2/Al_2O_3/AlN on Si under stressing current ranging from 5 to 100 mA.

Downloaded on 2015-06-08 to IP 155.69.250.85 address. Redistribution subject to ECS terms of use (see ecsdl.org/site/terms_use) unless CC License in place (see abstract).

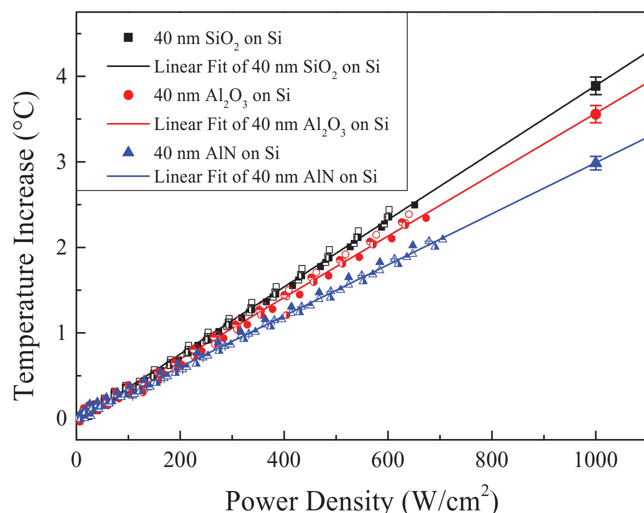

Figure 12. Temperature increase in RTD formed on 40 nm SiO_2/Al_2O_3/AlN on Si as a function of supplied power density.

bonded samples are 3.89 ± 0.10 and 3.56 ± 0.10°C, respectively. As compared to the traditional bonding material SiO_2, there is around 23% improvement in heat dissipation capability by using AlN as the bonding layer. This result experimentally proves that the AlN has the best heat dissipation capability among these three bonding materials studied here. The relatively low improvement in heat dissipation capability by using AlN, comparing to the expectation, is attributed to the poor quality of sputtered film and the presence of AlNO bonding interface serving as a barrier for heat dissipation. Moreover, the stack structure used in this demonstration is also responsible for it, where the RTDs are formed on top of 40 nm bonding layer/650 μm-thick Si. In this case, the Si substrate plays a dominant role in the heat dissipation. However, the improvement in heat dissipation is expected to be more significant when applying AlN in other bonding cases, such as III-V wafer bonding and Ge wafer bonding, as these semiconductor materials have much lower thermal conductivity than Si.[37,38]

Conclusions

In conclusion, a successful void-free AlN-AlN layer bonding was demonstrated on 150 mm Si wafer. Characterization results verified that the sputtered film was AlN, which was clean, smooth and with only approximately 5 nm partially oxidized top surface. The surface of the activated AlN thin film is verified to compose of substoichiometric nitrogen bound to aluminum, Al-O and Al-OH bonds, based on XPS spectra. The results have shown that a respectable AlN-AlN bonded interface is achieved with very few unbonded areas. The bond strength reached 1527.8 ± 272.2 mJ/m^2 with the addition of 3 hr bond strengthening annealing at 300°C. After the annealing, no obvious void enlargement or new void formation was observed, which was in virtue of sufficient outgassing during the pre-annealing step. Furthermore, the bonded AlN-AlN layer showed superior heat dissipation capability based on COMSOL multi-physic simulation and experimental results.

Acknowledgments

This research was supported by the National Research Foundation Singapore through the Singapore MIT Alliance for Research and Technology's "Low Energy Electronic Systems (LEES) IRG" research. Authors are grateful for the support provided by the management and technical staff in the Nanyang Nanofabrication Center at NTU. C. S. Tan is affiliated with Si-COE and NOVITAS at NTU.

References

1. U. Gösele and Q.-Y. Tong, *Annu. Rev. Mater. Sci.* **28**, 215 (1998).
2. G. Taraschi, A. J. Pitera, and E. A. Fitzgerald, *Solid. State. Electron.* **48**, 1297 (2004).
3. J. B. Lasky, *Appl. Phys. Lett.* **48**, 78 (1986).
4. Y. Li, S. Wang, B. Sun, H. Chang, W. Zhao, X. Zhang, and H. Liu, *ECS Trans.*, **50**, 303 (2013).
5. Q.-Y. Tong, C. Giho, R. Gafiteanu, and U. Gösele, *J. Microelectromech. Syst.*, **3**, 29 (1994).
6. C. J. Tracy, P. Fejes, N. D. Theodore, P. Maniar, E. Johnson, A. J. Lamm, A. M. Paler, I. J. Malik, and P. Ong, *J. Electron. Mater.*, **33**, 886 (2004).
7. A. Asadollahi, H. Radamson, T. Zabel, P. E. Hellstrom, and M. Ostling, in *15th Int. Conf. ULIS*, p. 81 (2014).
8. L. Liepvre, in *9th Int. Conf. on Group IV Photon. (GFP)*, p. 54 (2012).
9. M. Yokoyama, R. Iida,Y. Ikku, S. Kim, H. Takagi, T. Yasuda, H. Yamada, O. Ichikawa, N. Fukuhara, M. Hata, M. Takenaka, and S. Takagi, *Semicond. Sci. Technol.*, **28**, 094009 (2013).
10. R. L. Puurunen, T. Suni, O. Ylivaara, H. Kondo, M. Ammar, T. Ishida, H. Fujita, A. Bosseboeuf, S. Zaima, and H. Kattelus, in *16th Int. Conf. Solid-State Sens. Actuators and Microsystems (TRANSDUCERS)*, p. 978 (2011).
11. S. J. Koester, C. L. Schow, L. Schares, G. Dehlinger, J. D. Schaub, F. E. Doany, and R. A. John, *J. Light. Technol.*, **25**, 46 (2007).
12. J. F. Damlencourt, Y. Campidelli, T. Nguyen, B. Vincent, C. Le Royer, Y. Morand, S. Cristoloveanu, and L. Clavelier, *ECS Trans.*, **6**, 65 (2007).
13. J.-M. Fedeli, B. Ben Bakir, N. Olivier, P. Grosse, L. Grenouillet, E. Augendre, P. Phillippe, K. Gilbert, D. Bordel, and J. Harduin, in *Proc. SPIE 7942, Optoelectronic Integrated Circuits XIII*, 79420O (2011).
14. G. Roelkens, L. Liu, D. Liang, R. Jones, A. Fang, B. Koch, and J. Bowers, *Laser Photon. Rev.*, **4**, 751 (2010).
15. S. Keyvaninia, G. Roelkens, D. Van Thourhout, C. Jany, M. Lamponi, A. Le Liepvre, F. Lelarge, D. Make, G.-H. Duan, and D. Bordel, *Opt. Express*, **21**, 3784 (2013).
16. S. Bengtsson, M. Choumas, W. P. Maszara, M. Bergh, C. Olesen, U. Sodervall, and A. Litwin, in *Proc. 1990 IEEE SOS/SOI Technology Conf.*, p. 35 (1994).
17. D. Liang, M. Fiorentino, S. T. Todd, G. Kurczveil, R. G. Beausoleil, and J. E. Bowers, *Photonics Technol. Lett. IEEE.* **23**, 657 (2011).
18. R. L. Puurunen, T. Suni, O. M. E. Ylivaara, H. Kondo, M. Ammar, T. Ishida, H. Fujita, A. Bosseboeuf, S. Zaima, and H. Kattelus, *Sensors Actuators A.*, **188**, 268 (2012).
19. M. H. Park and S. H. Kim, *Mater. Sci. Semicond. Process.*, **15**, 6 (2012).
20. H. Morkoç, *Handbook of Nitride Semiconductors and Devices, Materials Properties, Physics and Growth*, Vol. 1, p. 62, Wiley-VCH Verlag GmbH & Co. KGaA, Weinheim (2009).
21. N. Bresson, S. Cristoloveanu, C. Mazuré, F. Letertre, and H. Iwai, *Solid. State. Electron.*, **49**, 1522 (2005).
22. C. Men, Z. Xu, Z. An, P. K. Chu, Q. Wan, X. Xie, and C. Lin, *Appl. Surf. Sci.*, **199**, 287 (2002).
23. W. Maszara, B. L. Jiang, A. Yamada, G. Rozgonyi, H. Baumgart, and A. De Kock, *J. Appl. Phys.*, **69**, 257 (1991).
24. C. S. Tan, D. F. Lim, S. G. Singh, S. K. Goulet, and M. Bergkvist, *Appl. Phys. Lett.*, **95**, 192108 (2009).
25. S. Huang, Q. Jiang, S. Yang, C. Zhou, and K. J. Chen, *Electron Device Lett. IEEE*, **33**, 516 (2012).
26. M. Alevli, C. Ozgit, and I. Donmez, *Acta Phys. Pol. A.* **120**, 58 (2011).
27. T. Tsuchida and H. Takahashi, *J. Mater. Res.* **9**, 2919 (1994).
28. N. Laidani, L. Vanzetti, M. Anderle, a. Basillais, C. Boulmer-Leborgne, and J. Perriere, *Surf. Coatings Technol.*, **122**, 242 (1999).
29. J. F. Moulder, W. F. Stickle, P. E. Sobol, and K. D. Bomben, *Handbook of X-ray photoelectron spectroscopy*, p. 43, Perkin Elmer Corporation, Eden Prairie, MN (1992).
30. S. W. King, J. P. Barnak, M. D. Bremser, K. M. Tracy, C. Ronning, R. F. Davis, and R. J. Nemanich, *J. Appl. Phys.*, **84**, 5248 (1998).
31. S. J. Kerber, *J. Vac. Sci. Technol. A*, **14**, 1314 (1996).
32. Q.-Y. Tong, *Mater. Sci. Eng. B.* **87**, 323 (2001).
33. X. Ma, W. Liu, Z. Song, W. Li, and C. Lin, *J. Vac. Sci. Technol. B Microelectron. Nanom. Struct.* **25**, 229 (2007).
34. E. A. Chowdhury, J. Kolodzey, J. O. Olowolafe, G. Qiu, G. Katulka, D. Hits, M. Dashiell, D. Van der Weide, C. P. Swann, and K. M. Unruh, *Appl. Phys. Lett.*, **70**, 2732 (1997).
35. Q.-Y. Tong and U. Gösele, *J. Electrochem. Soc.* **143**, 1773 (1996).
36. Q.-Y. Tong, L.-J. Huang, and U. M. Gösele, *J. Electron. Mater.* **29**, 928 (2000).
37. C. Glassbrenner and G. Slack, *Phys. Rev.* **143**, A1058 (1964).
38. M. Holland, *Phys. Rev.* **478**, A471 (1964).

Downloaded on 2015-06-08 to IP 155.69.250.85 address. Redistribution subject to ECS terms of use (see ecsdl.org/site/terms_use) unless CC License in place (see abstract).